Journal of Materials Chemistry A

ROYAL SOCIETY OF CHEMISTRY

PAPER

View Article Online
View Journal | View Issue

Cite this: J. Mater. Chem. A, 2025, 13, 10736

Layered sodium vanadate (NaV_8O_{20}) nanobelts: a new high-performing pseudocapacitive material for sodium-ion storage applications†

Amol S. Vedpathak,[ab] Shrishreshtha A. Sahu,[c] Tanuja N. Shinde,[b] Shubham S. Kalyane,[b] Sambhaji S. Warule,[d] Ramchandra S. Kalubarme,[c] Aditya Narayan Singh,[e] Ravindra N. Bulakhe,*[f] Ji Man Kim *[f] and Shrikrishna D. Sartale *[b]

Multifunctional layered nanostructures have attracted great attention for next-generation electrochemical supercapacitors and metal-ion batteries. Herein, we use a hydrothermal method to demonstrate the synthesis of 1D and layered sodium vanadate (NaV_8O_{20}) nanobelts architecture. These NaV_8O_{20} nanobelts demonstrate outstanding electrochemical performance in supercapacitors (SCs) and sodium-ion batteries (SIBs). The possible formation mechanism of NaV_8O_{20} nanobelts is briefly discussed. Benefiting from the 1D and layered nanostructure, pre-inserted cations, significantly enhanced electrochemical conductivity, and high electroactive surface area, the prepared NaV_8O_{20} electrode material exhibited excellent charge storage capacity, favorable rate, and cyclic stability performance. The NaV_8O_{20} nanobelts displayed outstanding electrochemical characteristics, including 676 F g^{-1} of specific capacitance, 45 W h kg^{-1} of energy density and 5224 W kg^{-1} of power density. Additionally, on testing in Na-ion batteries, the NaV_8O_{20} nanobelts exhibit a discharge capacity of 110 mA h g^{-1} at 10 mA g^{-1} and retain ~52% capacity after 100 cycles. Along with this, the galvanostatic intermittent titration technique (GITT) measurements reveal a high diffusion coefficient for Na^+ ions, highlighting the efficient Na^+ ions transportation within the NaV_8O_{20} structure. To our knowledge, this is the first report on the use of NaV_8O_{20} nanobelts for both SIBs and SCs, marking a significant contribution to the development of multifunctional materials for energy storage applications.

Received 4th December 2024
Accepted 12th March 2025

DOI: 10.1039/d4ta08624d

rsc.li/materials-a

1. Introduction

The rapid advancement and proliferation of electrochemical energy storage (EES) technologies are reshaping modern life while laying the foundation for a sustainable energy future. The growing demand for portable/wearable electronics, electric vehicles, and stationary energy storage systems has sparked significant global interest in EES technologies, particularly supercapacitors (SCs) and metal-ion batteries (MIBs). These devices have emerged as critical components for addressing the energy challenges of modern technology due to their distinct capabilities in energy storage and power delivery.[1,2] However, to address the growing requirements for energy storage systems, the performance of these EES devices must be significantly improved. The working electrode material is one of the most essential parameters for EES applications.[3] Therefore, enhancing the charge storage capacity of electrode materials has become a primary focus in recent EES research. One-dimensional (1D) and layered nanostructures have garnered significant scientific and technical attention for EES systems, attributed to their high electroactive surface area, structural stability, short charge carrier transport pathways, and favorable intercalation/de-intercalation processes.[4] Various 1D and layered nanostructures, including carbon nanostructures, conducting polymers, metal phosphides and metal chalcogenides, have been investigated as potential electrode materials (both cathode and anode) for SC and MIB applications.[5–10] Among these, transition metal oxides (TMOs) stand out as highly

[a]Symbiosis Centre for Nanoscience and Nanotechnology, Symbiosis International (Deemed University), Pune 412115, India
[b]Thin Films and Nanomaterials Laboratory, Department of Physics, Savitribai Phule Pune University, Pune 411 007, India. E-mail: shrikrishna.sartale@unipune.ac.in
[c]Centre for Materials for Electronics Technology (C-MET), Panchavati, Off. Dr. Homi Bhabha Road, Pashan, Pune 411008, India
[d]Department of Physics, Nowrosjee Wadia College, Pune 411 001, India
[e]Department of Energy and Materials Engineering, Dongguk University-Seoul, Seoul, 04620, Republic of Korea
[f]Department of Chemistry, Sungkyunkwan University, Suwon, 440-746, Republic of Korea. E-mail: jimankim@skku.edu; bulakhe@skku.edu

† Electronic supplementary information (ESI) available: S1: (a) chemicals and reagents, (b) formulae for C_{sp} calculation of working electrode and ASC device, and (c) characterization techniques, S2: XPS studies of NaV_8O_{20} nanobelts sample, S3: electrochemical measurements of carbon paper, bulk V_2O_5 and NaV_8O_{20} electrode and Na ion battery, Table S1: crystallographic data of the NaV_8O_{20} powder obtained from Rietveld refinement, Table S2: C_{sp} values of NaV_8O_{20} electrode from CV curves, Table S3: C_{sp} values of NaV_8O_{20} electrode from GCD curves, Table S4: C_{sp}, energy and power density values of AC//NaV_8O_{20} ASC coin cell device. See DOI: https://doi.org/10.1039/d4ta08624d

favorable electrodes for EES due to their multifarious oxidation states, high theoretical specific capacitance, diverse 1D/2D nanostructured morphologies, high electroactive surface area, and cost-effective fabrication processes.[11–13]

Transition metal vanadates, a class of bimetallic TMOs, have gathered great scientific attention as electrode materials for SCs and MIBs. Their appeal stems from their high surface area, low-dimensional and layered structures, excellent pseudocapacitive properties, enhanced electrical conductivity, and superior cyclic stability. These characteristics enable rapid and reversible surface redox reactions of electroactive species, making them highly suitable for advanced energy storage applications.[14,15] Currently, different binary transition metal vanadates such as $Co_3V_2O_8$, $FeVO_4$, MnV_2O_8, $Ni_3V_2O_8$, and $Cu_3V_2O_8$ have proven their ability in SCs and MIBs applications owing to their wide working potential window, high specific capacitance, and energy storage capacity compared to their pristine metal oxide counterparts.[16–20] For example, quasi-cuboidal CoV_2O_6 has been shown to exhibit a specific capacitance of 223 F g^{-1} at 1 A g^{-1}, along with remarkable cyclic stability of 123% after 15 000 cycles, making it suitable for SC applications.[21] Similarly, 3D flower-like $Ni_3V_2O_8$@CNTs have proven effective in enhancing energy storage capacity due to their high specific capacitance of 1054 F g^{-1} at 1 A g^{-1} and retain high cyclic stability of 89% after 10 000 cycles.[22] Pseudocapacitive layered $Fe_5V_{15}O_{39}(OH)_9 \cdot 9H_2O$ nanosheets exhibit significant potential as a cathode material for lithium-ion batteries, achieving a high reversible capacity of 350 mA h g^{-1} at 100 mA g^{-1}, indicating its capability for long-term cycling stability.[23] Similarly, Zr–$NH_4V_4O_{10}$ has been identified as a promising cathode material for sodium-ion batteries, achieving a high specific capacity of 342 mA h g^{-1} at 100 mA g^{-1}, positioning it as an appealing option for large-scale energy storage systems.[24] However, despite these advancements, several challenges persist, including the complex synthesis procedures, use of toxic and hazardous materials and high cost of precursor materials, which hinder the feasibility of these materials for widespread industrial applications.[15] Due to its numerous significant benefits, the hydrothermal method is the most frequently utilized for synthesizing metal vanadates. This approach enables accurate regulation of the morphology and particle size of resultant nanostructures, which is essential for enhancing the electrochemical performance of energy storage devices. This process is environmentally friendly and scalable, capable of being conducted at relatively low temperatures and pressures, contributing to its energy efficiency and cost-effectiveness. Furthermore, the hydrothermal approach facilitates the creation of well-crystallised nanostructures that exhibit high purity, thereby improving their applicability in energy storage applications. Considering these aspects, low-cost and environment-friendly alkali metals (Li, Na, K) can be appropriate alternatives to toxic and expensive metals for developing metal vanadate materials. However, alkali metal-inserted vanadate materials have been less explored for electrochemical SC and MIB applications.

In this study, we address these above-mentioned challenges by developing a simple, cost-effective hydrothermal route to prepare the 1D and layered structural sodium vanadate (NaV_8O_{20}) nanobelts without any post-annealing treatment. Sodium vanadate is particularly gaining attention due to its pre-inserted sodium ions, which enhances electrochemical performance and its suitability as a low-cost charge storage material for SCs and sodium-ion battery (SIB) applications. To the best of our knowledge, no prior publication has been reported that explored the electrochemical SCs and sodium-ion battery (SIB) applications of the 1D and layered NaV_8O_{20} structures. Owing to the unique 1D layered structure and nanobelts morphology features, the NaV_8O_{20} electrode displayed outstanding electrochemical features with high specific capacitance (C_{sp}) and cyclic stability. The NaV_8O_{20} material was investigated using various electrochemical and physicochemical characterization techniques to evaluate its structural, morphological and electrochemical characteristics. We have also successfully demonstrated the practical applicability of NaV_8O_{20} nanobelts in electrochemical applications, particularly in solid-state asymmetric SCs, highlighting their potential for advanced EES systems.

2. Experimental section

2.1 Synthesis of NaV_8O_{20} nanobelts

The details of chemicals and reagents are provided in ESI, S1(a).† The chemicals and reagents used for all the experiments were of analytical grades. A hydrothermal method was used to synthesize NaV_8O_{20} material (Fig. 1a). First, 0.75 g of V_2O_5 powder was dispersed in 40 ml of double distilled water and ultrasonicated for 90 min. Then, with continuous stirring, 1 M Na_2SO_4 (30 ml) aqueous solution was gradually added to the V_2O_5 suspension. After 30 min, the mixture was transferred into a 100 ml Teflon-lined stainless-steel autoclave and heated to 180 °C for 48 h. After hydrothermal treatment, the obtained greenish-colored product was washed several times with double distilled water. Finally, the obtained product was dried at 150 °C in a vacuum oven.

2.2 Preparation of working electrode, AC//NaV_8O_{20} asymmetric SC and Na-ion battery

The schematic representation of the working electrode fabrication *via* the slurry casting method is illustrated in Fig. 1b. Initially, a homogeneous slurry was prepared by mixing NaV_8O_{20} nanobelts (active material), polyvinylidene difluoride (PVDF) as a binder, and activated carbon (AC) as a conductive additive in a weight ratio of 8 : 1 : 1, using *N*-methyl-pyrrolidone (NMP) as the solvent. This slurry was then uniformly coated onto a Toray carbon paper substrate. The coated electrode was subsequently dried under vacuum at 150 °C for 24 hours. The final electrode had an active surface area of 1 × 1 cm^2, with a mass loading of ~1.2 mg.

Fig. 1c and d depicts the schematic for the device manufacture processes for SC and SIB coin cells of the NaV_8O_{20} nanobelts material. As shown in Fig. 1c, the AC//NaV_8O_{20} asymmetric SC (ASC) device was fabricated using NaV_8O_{20} nanobelts as cathode (~1.2 mg of mass loading) and AC as an anode (~2 mg of mass loading) materials prepared onto a circular 16 mm carbon paper current collector. These electrodes were separated using a cellulose membrane. The PVA–$NaClO_4$ gel electrolyte was prepared by mixing 2 g $NaClO_4$ and 2 g PVA in 25 ml DDW and then heated at 80 °C for 3 h. Finally, the AC//NaV_8O_{20} asymmetric SC device was

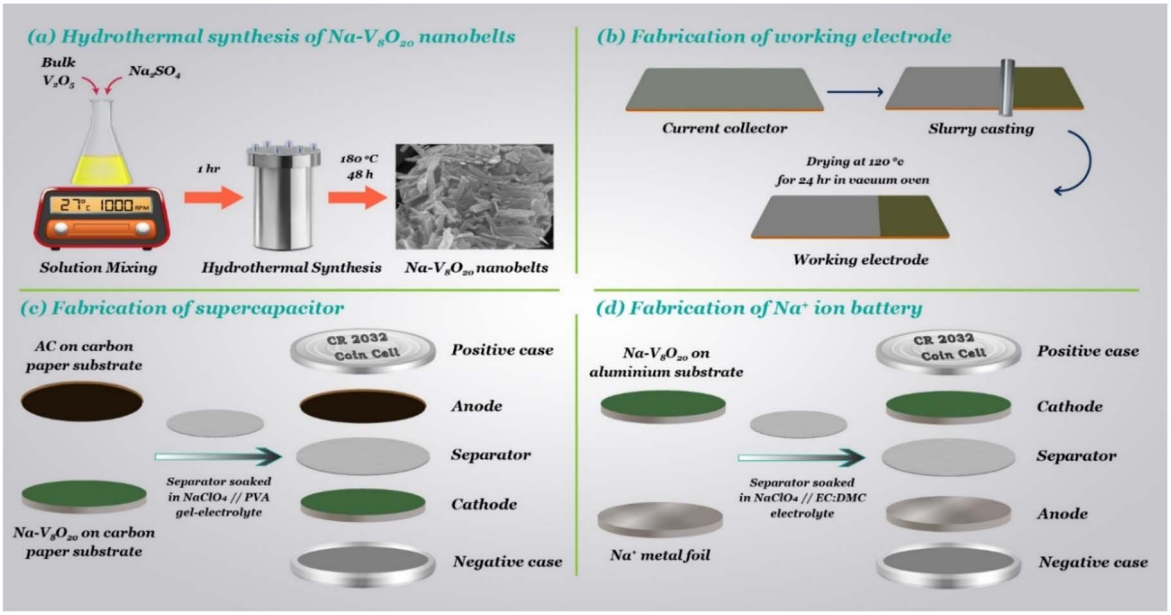

Fig. 1 Schematic representation of (a) hydrothermal synthesis of NaV_8O_{20} nanobelts, (b) preparation of working electrode, (c) fabrication of ASC device and (d) fabrication of Na-ion battery.

fabricated with a CR2032 coin cell using the PVA–$NaClO_4$ gel electrolyte.

The sodium-ion storage performance of NaV_8O_{20} nanobelts as the active cathode material was investigated. The electrode was fabricated by combining NaV_8O_{20}, PVDF, and AC with a weight ratio of 8 : 1 : 1 and thoroughly mixed in NMP solvent. The prepared homogeneous slurry was uniformly coated onto a current collector (aluminium foil) using the doctor blade method and subsequently dried under a vacuum oven at 100 °C for 12 hours. The dried film was then cut into 16 mm diameter discs with a mass loading of approximately 0.745 mg cm^{-2}. Sodium metal was utilized as the counter and reference electrode, while a 19 mm diameter glass-fiber Whatman separator was employed. The 2032-type coin cells were assembled in an argon-filled glove box, where oxygen and moisture levels were controlled at 0.1 ppm. A 1 M solution of $NaClO_4$ in ethylene carbonate (EC) and diethyl carbonate (DEC) (1 : 1 v/v), with the addition of 5% fluoroethylene carbonate (FEC), was used as the electrolyte. A schematic representation of the Na^+ ion battery assembly process is provided in Fig. 1d.

2.3 Electrochemical measurements

All the electrochemical measurements of electrodes and fabricated devices, such as cyclic voltammetry (CV), galvanostatic charging–discharging (GCD), electrochemical impedance spectroscopy (EIS), rate capability, and cycling stability tests were conducted on the IVIUM-Vertex 1A electrochemical workstation (Ivium Technologies, Netherlands).

2.4 Physicochemical characterization of 1D and layered nanostructured NaV_8O_{20} nanobelts

The physicochemical characteristics of the synthesized material were investigated using various techniques, including X-ray diffraction (XRD), Brunauer–Emmett–Teller (BET) surface area analysis, field emission scanning electron microscopy (FESEM), transmission electron microscopy (TEM), and X-ray photoelectron spectroscopy (XPS). Further details regarding these methods are provided in the ESI, S1(b).†

3. Results and discussion

3.1 XRD studies

XRD characterization was carried out to identify the crystal structure and phase purity of the NaV_8O_{20} material. Fig. 2a shows the comparative XRD pattern of bulk V_2O_5 and NaV_8O_{20} powders. The diffraction pattern of bulk V_2O_5 powder displays sharp and intense diffraction peaks, which match well to α-V_2O_5 phase (JCPDS no. 77-2418) with an orthorhombic crystal structure. By comparing both the diffraction patterns, it is clear that, after hydrothermal treatment, the V_2O_5 phase is converted into the newly formed NaV_8O_{20} phase. In the XRD pattern of NaV_8O_{20} powder, all the observed peaks are consistent with the characteristic peaks of the NaV_8O_{20} phase (JCPDS no. 45-1363) with a monoclinic crystal structure. Furthermore, no additional diffraction peaks related to V_2O_5 or any other sodium vanadate phases were observed, implying the high phase purity of the NaV_8O_{20} phase. However, the NaV_8O_{20} phase displays relatively low-intensity and broad diffraction peaks compared with bulk V_2O_5, corresponding to the small crystallite size and low crystallinity of the NaV_8O_{20} nanobelts material. The intense diffraction from the (001) plane illustrates the preferential orientation of the NaV_8O_{20} phase in the *c* direction, which possesses the layered crystal structure arrangement.[25] The interlayer spacing (*d*-value) estimated from the (001) diffraction peak was ~10 Å. This large interlayer spacing is favorable for accommodating Na^+ ions during electrochemical processes.

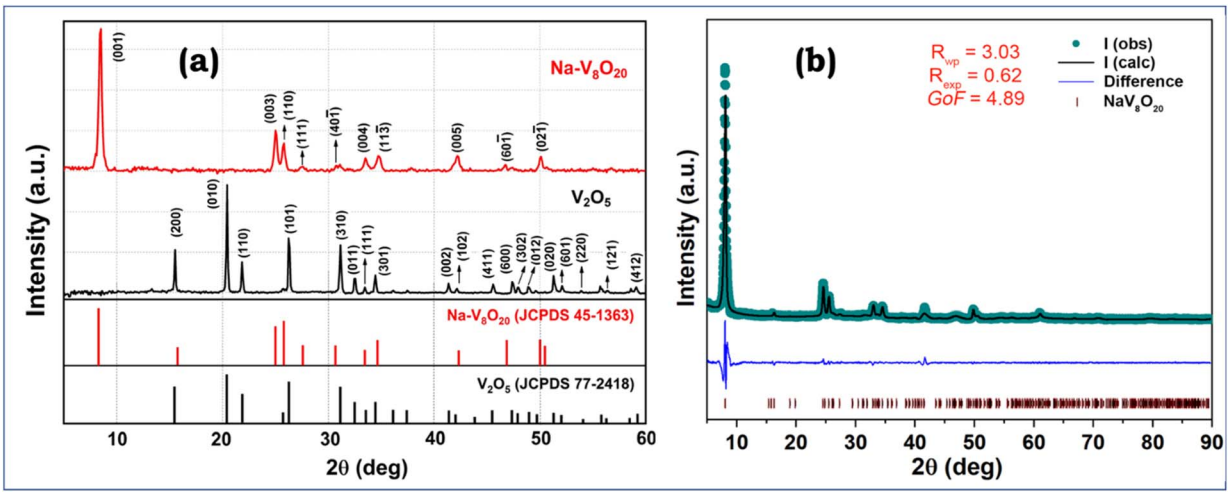

Fig. 2 (a) XRD patterns of V_2O_5 and NaV_8O_{20} powder samples and (b) XRD refinement analysis of NaV_8O_{20} powder sample.

Rietveld refinement of the NaV_8O_{20} phase was conducted to identify the position of the sodium ions in the NaV_8O_{20} phase. Fig. 2b depicts the Rietveld refinement analysis of the NaV_8O_{20} nanobelts, performed using the MAUD software. The XRD pattern of the NaV_8O_{20} sample was fitted using the standard crystallography information file (CIF) consisting of

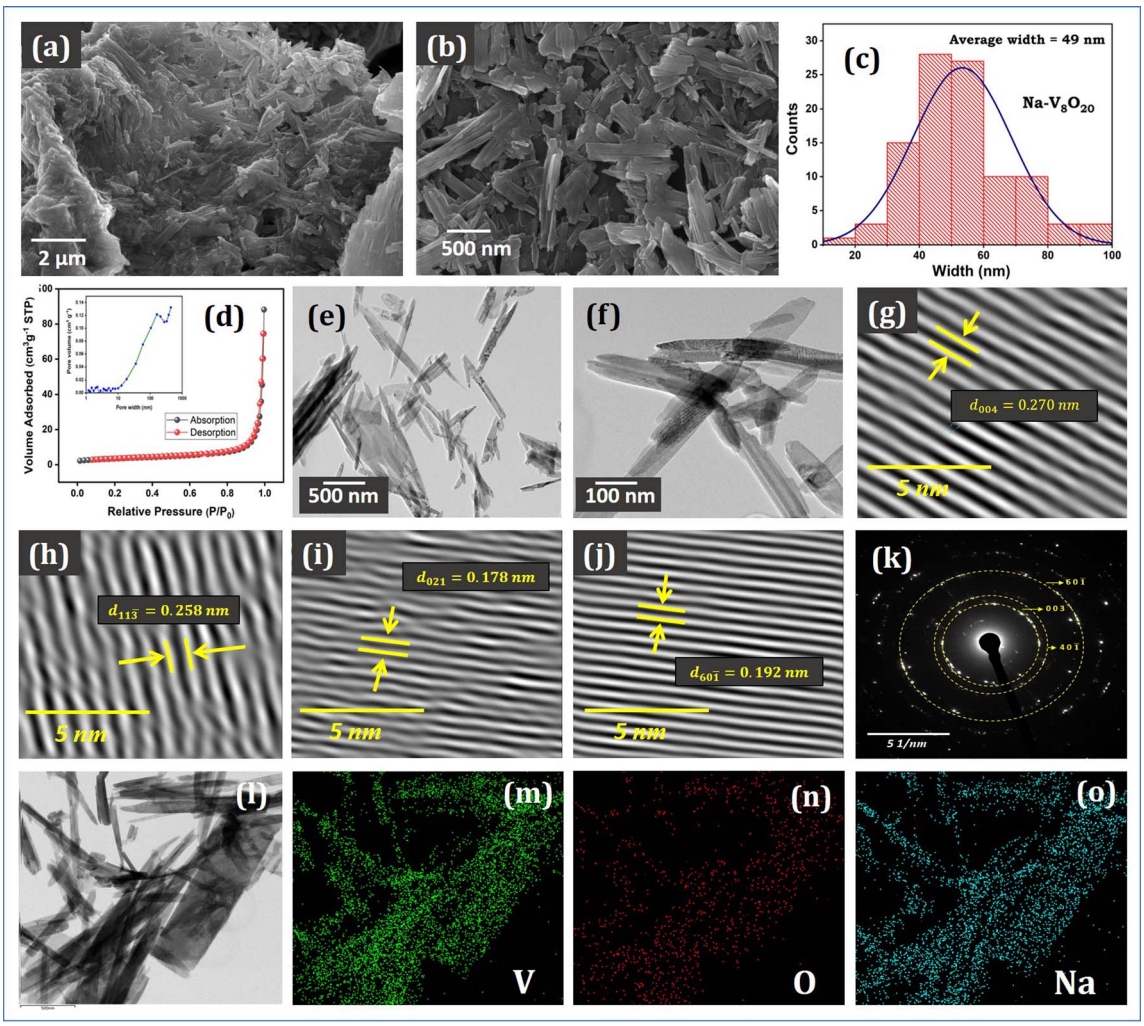

Fig. 3 (a and b) FESEM images, (c) histogram for average width; (d) N_2 adsorption/desorption isotherms; (e and f) TEM images, (g–j) HR-TEM images, (k) SAED pattern and (l–o) elemental mapping of NaV_8O_{20} nanobelts.

$(Na,Ca)(V,Fe)_8O_{20}\cdot nH_2O$ and JCPDS no. 45-1363.[26] By replacing the Ca and Fe atomic sites with corresponding amounts of Na and V, the refined analysis resulted in good agreement factors ($R_{wp} = 3.03$, $R_{exp} = 0.62$ and goodness of fit, GoF = 4.89). The parameters that are refined are (1) microstructure, (2) basic phase parameters, (3) background and scale parameters, and (4) crystal structure (lattice parameter, occupancy, fractional coordinate, and isotropic displacement factor, B_{iso}). The refined lattice parameters are: $a = 11.74(2)$ Å, $b = 3.6600(6)$ Å, and $c = 11.117(5)$ Å with monoclinic phase, $C2/m$ space group and β angle value = 102.4(1)°. The refinement data are mentioned in the ESI, Table S1.†

3.2 FE-SEM, BET and TEM studies

The morphological properties of NaV_8O_{20} material were elucidated by FESEM techniques (Fig. 3a and b). The low-resolution FESEM image (Fig. 3a) shows a network of uniformly distributed nanobelts adjoining each other to establish the self-assembled architecture of NaV_8O_{20} nanobelts. This 1D and densely attached nanobelt morphology will be favorable for electron transportation and will help to enhancing the diffusion of Na^+ ions by serving maximum electroactive sites during the electrochemical interactions.[27,28]

Fig. 3b represents the high-resolution FESEM image of the NaV_8O_{20} nanobelts. The width of NaV_8O_{20} nanobelts was measured using ImageJ software and the Gaussian function was used to calculate the average width of nanobelts. The calculated average width (Fig. 3c) of the NaV_8O_{20} nanobelt was ~49 nm. Additionally, to identify the surface area and pore size of the NaV_8O_{20} nanobelts sample, N_2 adsorption/desorption isotherm analysis was used. Fig. 3d shows the mesopores nature of NaV_8O_{20} nanobelts with a specific surface area of 12.41 $m^2\ g^{-1}$ and pore size of ~43.3 nm (inset of Fig. 3d). Furthermore, crystallinity, morphological and elemental analysis of the NaV_8O_{20} nanobelts sample was investigated through TEM analysis. The low and high-magnification TEM images (Fig. 3e and f) display the nanobelts-like morphology of the NaV_8O_{20} material. The corresponding HRTEM images (Fig. 3g–i) depict the well-observable lattice fringes. The measured d-spacings of 0.22, 0.45, and 0.36 nm correspond to the (204), (201), and (003) lattice planes of the NaV_8O_{20} nanobelts. The selected area electron diffraction (SAED) pattern (Fig. 3k) further confirms the crystallinity of the NaV_8O_{20} nanobelts, revealing their polycrystalline nature. Furthermore, the elemental mapping images (Fig. 3l–o) show a uniform spreading of Na, V, and O elements all over the NaV_8O_{20} nanobelts surface.

The X-ray photoelectron spectroscopy analysis of the NaV_8O_{20} nanobelts sample is provided in the ESI, S2.†

3.3 Formation mechanism of NaV_8O_{20} nanobelts

The possible formation mechanism of the NaV_8O_{20} nanobelts (Fig. 4) can be proposed based on their 1D nanobelt morphology and layered crystal structure, as confirmed by structural and morphological characterizations.

A hydrothermal synthesis route was used to prepare 1D and layered NaV_8O_{20} nanobelts. In the typical synthesis procedure, bulk V_2O_5 powder (vanadium precursor) was pre-treated with ultrasonication in double distilled water to break bulk vanadium particles into smaller particles. This ultrasonication process promotes the dissociation and formation of free vanadium ionic species such as decavanadate ($[V_{10}O_{28}]^{6-}$), polyoxovanadate ($V_8O_{20}{}^{4-}$), vanadyl ions (VO^{2+}), hydrated vanadium species *etc.*, because of partial reduction and condensation of vanadium.[29,30]

Here, the presence of water plays a vital role in the hydrolysis of V_2O_5. When Na_2SO_4 is added to the ionic solution of vanadium, the Na^+ ions interact with $V_8O_{20}{}^{4-}$ ions, forming hydrated sodium vanadate complexes. Here, the free sulfate ions ($SO_4{}^{2-}$) do not participate directly in the formation of the final product and water molecules (crystal water) help to stabilize these complexes by maintaining charge balance, leading to the formation of the $NaV_8O_{20}\cdot 2H_2O$ (complex), where water integrates sodium ions into the polyvanadate structure.

During the hydrothermal treatment, the system is subjected to high temperature and pressure, promoting dehydration and crystallization. The removal of crystal water during this step drives the organization of sodium vanadate species into well-defined and layered nanobelt structures. The dehydration process facilitates the reorganization of the vanadate layers, promoting anisotropic and preferentially growth NaV_8O_{20} nanobelts along the c direction, confirmed by XRD with an intense peak at 8.8° with Miller indices (001).

Afterward, the FESEM image reveals that the NaV_8O_{20} nanobelts adopt a self-assembled morphology. This may be due to the removal of crystal water during crystallization, facilitating the formation of smooth, well-defined nanobelts. The self-assembly process is further driven by the depreciation of structural energy during crystallization, with sodium ions playing a role in charge stabilization.[31]

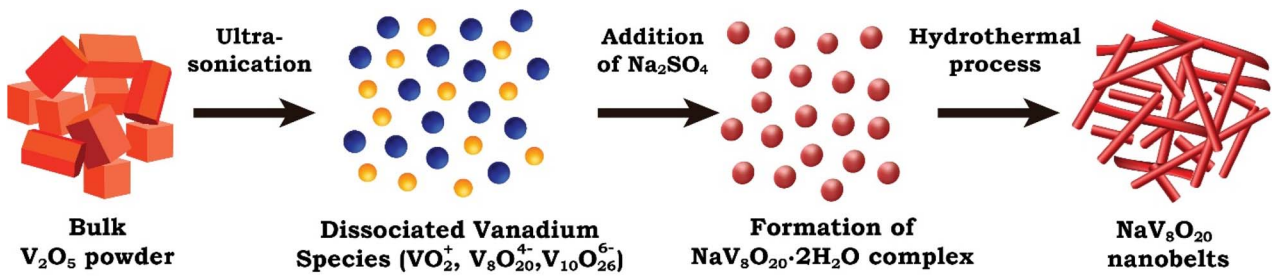

Fig. 4 Schematic representation for the possible formation mechanism of NaV_8O_{20} nanobelts.

4. Electrochemical investigation

4.1 Electrochemical performance of NaV_8O_{20} nanobelts electrode

The electrochemical charge storage features of the NaV_8O_{20} electrode material for supercapacitor studies were evaluated in 1 M Na_2SO_4 electrolyte within a 0 to 0.6 V voltage window. The CV curves of the NaV_8O_{20} electrode were recorded for various scan rates ranging from 2.5 to 50 mV s^{-1}, as shown in Fig. 5a. In Fig. 5a, the CV curves of the NaV_8O_{20} electrode exhibit a typical extrinsic pseudocapacitive nature consisting of a nearly rectangular shape with broad oxidation and reduction peaks. This extrinsic pseudocapacitive nature mainly arises from surface faradaic charge transfer reactions due to the intercalation or diffusion of charge-compensating electrolyte ions.[32] However, this nature is well retained despite decreasing the scan rate up to 2.5 mV s^{-1}, implying outstanding rate performance of the NaV_8O_{20} electrode in Na_2SO_4 aqueous solutions. From the CV curves, the C_{sp} values for different scan rates of the NaV_8O_{20} electrode were calculated using eqn (E1) (ESI, S1(b)†) and are given in the ESI, Table S2.†

The CV curves of the NaV_8O_{20} electrode reveal a hybrid charge storage behaviour, combining pseudocapacitive and electric double-layer (EDLC) characteristics. The Trasatti method is employed to understand the charge storage mechanism of the NaV_8O_{20} nanobelts. This method helps distinguish between the contributions of surface-capacitive and diffusion-controlled processes. According to Trasatti, the overall capacitance arises from a blend of these two mechanisms: surface capacitive reactions and diffusion-driven charge storage.[33,34] Fig. 5b depicts the Trasatti plot, plotted using C_{sp} against the square root of the scan rate. The *y*-axis intercept of the linear fit represents the surface-controlled contribution. Based on this intercept, the proportion of surface capacitive and diffusion-controlled charge storage components was calculated across various scan rates. These results are displayed in Fig. 5c as a histogram. This histogram shows that the surface capacitive (EDLC) contribution has the dominant charge storage mechanism over the diffusion-controlled contribution. By increasing the scan rate from 2.5 to 50 mV s^{-1}, the surface capacitive contributions improved from 56 to 85% with no noticeable CV curve distortion detected, revealing a better rate performance of the NaV_8O_{20} electrode. Furthermore, at lower scan rates (2.5 to 20 mV s^{-1}), broad redox peaks and quasi-rectangular CV curves were observed (ESI, Fig. S3(d)†). This is due to surface faradaic reactions, clarifying the extrinsic pseudocapacitive nature.

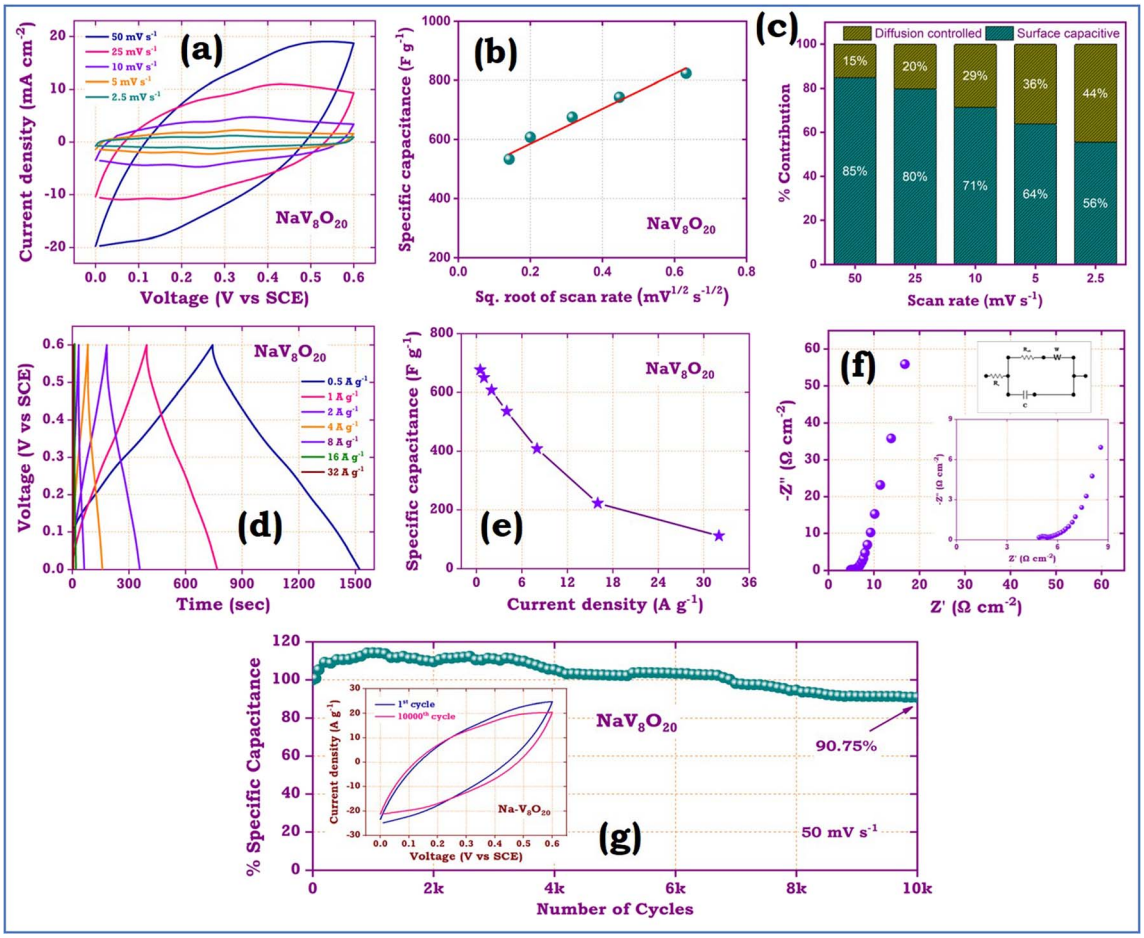

Fig. 5 (a) CV curves, (b) C_{sp} from CV curves *versus* square root of scan rate, (c) histogram for charge storage contribution; (d) GCD profile; (e) plot of C_{sp} *vs.* current density; (f) Nyquist plots and (g) cyclic stability of NaV_8O_{20} electrode.

During the cathodic CV scans (ESI, Fig. S3(d)†), two reduction peaks at ~0.2 and ~0.35 V *vs.* SCE arose because of the reduction of vanadium ionic species from $V^{5+} \rightarrow V^{4+}$ and $V^{4+} \rightarrow V^{3+}$. Whereas, in the anodic CV scans, two oxidation peaks at ~0.1 and ~0.24 V *vs.* SCE were detected due to the oxidation of vanadium ionic species from $V^{3+} \rightarrow V^{4+}$ and $V^{4+} \rightarrow V^{5+}$. Interestingly, by increasing the scan rates, the cathodic peaks gradually shifted towards the higher potentials, indicating that rapid and scan rate-dependent redox reactions occurred near the NaV_8O_{20} electrode surface.[35] Fig. 5d shows the GCD curves of the NaV_8O_{20} electrode, performed 0.5 to 32 A g^{-1} of current densities. All the GCD curves show an ideal triangular and symmetric nature with a slight hump at ~0.4 V *vs.* SCE, which indicates fast faradaic reactions and high reversibility of Na^+ ions on the NaV_8O_{20} electrode surface. Additionally, the GCD curves show extended charging–discharging characteristics with a negligible *iR* drop, signifying the outstanding rate capability. The C_{sp} values were calculated using eqn (E2) (see ESI†) and summarized in the ESI, Table S3.† The NaV_8O_{20} electrode displays an optimal C_{sp} of 676 F g^{-1} at a current density of 0.5 A g^{-1}; afterwards, it decreases with an increase in current density (as shown in Fig. 5e). At a 32 A g^{-1} current density, the NaV_8O_{20} electrode still provides the admirable C_{sp} of 142 F g^{-1}. We believe these excellent C_{sp} values mainly arise from the pre-insertion of Na^+ into the V_8O_{20} structure, which offers a high electroactive surface area, enhances the overall electronic conductivity and simplifies the Na^+ ions insertion/de-insertion process. The electrode material's low electric and electrochemical resistances are typically preferred for the supercapacitor's longer cyclic lifespan and versatile applicability. The electrochemical resistance characteristics of the NaV_8O_{20} electrode material were evaluated through EIS measurements. The Nyquist plot for the NaV_8O_{20} electrode is presented in Fig. 5f. In the high-frequency region of the Nyquist plot, two key components are observed: the equivalent series resistance (R_s) and the charge transfer resistance (R_{ct}). R_s represents the overall internal (ohmic) resistance, which encompasses the active electrode material's intrinsic resistance, the electrolyte's ionic resistance, and the contact resistance at the electrode/electrolyte interface.[36–38] Meanwhile, the diameter of the semicircle represents the charge transfer resistance, which is associated with faradaic reactions. The simulated circuit provided that the NaV_8O_{20} electrode possesses $R_s = 4.9\ \Omega$ and $R_{ct} = 0.55\ \Omega$. These low resistance values are attributed to the high electronic conductivity, large electroactive surface area, enhanced electron transport rate, and reduced charge transfer resistance of the NaV_8O_{20} electrode, which collectively enable rapid faradaic reactions at the electrode/electrolyte interface. In the Nyquist plot, the Warburg impedance (W) is associated with the vertical line in the low-frequency region, corresponding to the intercalation or diffusion of electrolyte ions inside the active electrode material. The slope of the Warburg impedance approaches a 90° angle, signifying the capacitive behaviour of the NaV_8O_{20} electrode.

Long cyclic life is one of the significant parameters for electrochemical supercapacitor applications. The electrochemical cycling stability over the NaV_8O_{20} electrode (Fig. 5g) was performed at a scan rate of 50 mV s^{-1} over 10 000 cycles. In the initial ~1000 cycles, the C_{sp} gradually increases and then tends to stabilize for further CV cycling. This is because of the activation of the NaV_8O_{20} electrode through the insertion/de-insertion of Na^+ ions and complete infiltration of Na^+ electrolyte ions inside the active electrode material surface.[21] The NaV_8O_{20} electrode retains 90% of its initial C_{sp} after 10 000 CV cycles. This outstanding cycling stability is mainly ascribed to the layered and 1D nanobelts structured assembly of the NaV_8O_{20} electrode, which offers significant redox active sites and efficiently accommodates the possible volume deviations through Na^+ ions insertion/de-insertion process, which ultimately enhances the charge storage capacity of the NaV_8O_{20} electrode material.

4.2 Electrochemical performance of the AC//NaV_8O_{20} asymmetric supercapacitor (ASC) device

To evaluate the practical applications of the NaV_8O_{20} nanobelts for supercapacitors, the AC//NaV_8O_{20} ASC coin cell device (Fig. 1d) was fabricated. Before the fabrication of the SC device, the NaV_8O_{20} (cathode) and AC (anode) were electrochemically evaluated in a three-electrode system to assess the appropriate working voltage window.

Fig. 6a shows the CV profile for the AC and NaV_8O_{20} electrodes carried out in a three-electrode system at a scan rate of 50 mV s^{-1} in 1 M Na_2SO_4 electrolyte. The CV curves of NaV_8O_{20} and AC electrodes are nearly rectangular, measured between the voltage windows of 0 to 0.6 V *vs.* SCE and −1 to 0 V *vs.* SCE, respectively. These results imply that integrating the cathode and anode can provide a 1.6 V working voltage. After the fabrication of the ASC device, first, CV measurements with different voltages from 1 to 1.6 V (Fig. 6b) were performed, which indicates the actual working voltage can be extended up to 1.6 V without showing any alteration in CV curves due to aqueous electrolyte redox processes. Fig. 6c displays the CV curves of the AC//NaV_8O_{20} ASC device, measured at 10 to 100 mV s^{-1} scan rates. These CV curves retain the quasi-rectangular shape observed for NaV_8O_{20} nanobelts electrodes in a three-electrode setup, confirming the pseudocapacitive behaviour of NaV_8O_{20} nanobelt material. Fig. 6d displays the GCD curves of the AC//NaV_8O_{20} ASC device measured at 0.5 to 16 A g^{-1} of current densities, demonstrating good symmetric and triangular GCD curves because of the high reversible charge/discharge processes. The C_{sp} of the AC//NaV_8O_{20} ASC device (ESI, Table S3†) was calculated using eqn (E2) (ESI†). Fig. 6e shows the change in C_{sp} with current densities. The highest C_{sp} of 126 F g^{-1} was achieved at 0.5 A g^{-1} of current density. Energy (E_d) and power densities (P_d) of the AC//NaV_8O_{20} ASC device were calculated using the following equations:[39]

$$E_d = \frac{C_{sp} \times (\Delta V)^2}{2 \times 3.6} \quad (1)$$

$$P_d = \frac{E}{\Delta t} \times 3600 \quad (2)$$

where, C_{sp} is the specific capacitance of the ASC device (F g^{-1}), ΔV is the voltage window, and Δt is the discharging time of the ASC device. Fig. 6f depicts the Ragone plot of the fabricated ASC

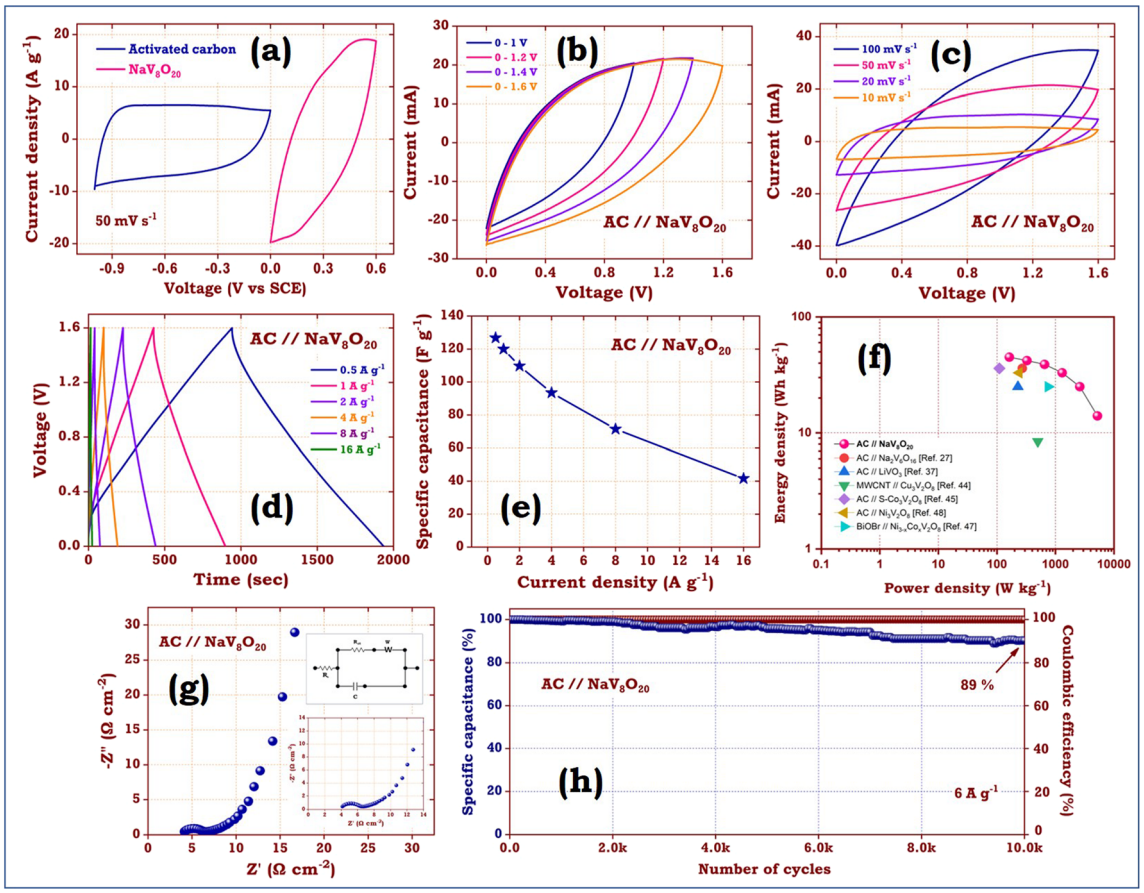

Fig. 6 (a) AC and NaV_8O_{20} electrodes CV curves in the three-electrode system, (b) CV curves for different voltage windows and (c) for different scan rates; (d) GCD curves for different current densities; (e) C_{sp} *vs.* current densities; (f) Ragone plot; (g) Nyquist Plot and (h) cyclic stability of AC//NaV_8O_{20} ASC device.

coin cell device. The AC//NaV_8O_{20} ASC device shows the highest E_d of 45 W h kg^{-1} at P_d of 163.26 W kg^{-1} and the highest P_d of 5224.48 W kg^{-1} at E_d of 14.8 W h kg^{-1} (ESI, Table S4†), which is higher than reported supercapacitor devices, as shown in Table 1. The resistive characteristics of the AC//NaV_8O_{16} ASC device were evaluated by EIS measurement. The Nyquist plot and the equivalent circuit for the ASC device are shown in Fig. 6g. The AC//NaV_8O_{20} ASC device displays $R_s = 3.8$ and $R_{ct} = 2.9$ Ω. The cyclic life of the SC is considered a key parameter for its long-term applicability in portable electronic devices. Therefore, the cyclic stability of the AC//NaV_8O_{20} ASC device was evaluated at a current density of 6 A g^{-1} for 10 000 cycles and presented in Fig. 6h. The AC//NaV_8O_{20} ASC device displayed 89% of its initial capacitance value with ~98% coulombic efficiency. This good cyclic stability can be accredited to (1) the proper combination of faradaic and pseudocapacitive electroactive material, (2) the appropriate interlayer spacing of the electrode materials, and (3) the large surface area of both electrode materials.

A detailed comparative analysis of the NaV_8O_{20} nanobelts developed in this study with the various metal vanadate electrodes for SC devices previously reported in the literature is presented in Table 1.

The comparative results suggest that, compared with reported metal vanadate electrode materials, the NaV_8O_{20} nanobelts consistently demonstrate better electrochemical performance. The NaV_8O_{20} nanobelts exhibit significantly higher capacitance with an operating window of 1.6 V, surpassing many vanadium-based alternatives. They offer excellent cyclic stability, retaining their electrochemical performance over 10 000 cycles, making them ideal for high-performance applications. Here, the key contributor to this exceptional electrochemical performance is the use of the Na_2SO_4 electrolyte, which provides numerous advantages, such as high ionic conductivity, high ionic mobility, and less corrosive compared to KOH. It also ensures compatibility with the Na^+ pre-insertion in the electrode material, allowing for efficient ion transfer and enhanced electrochemical reactions. Moreover, the excellent electrochemical performance of the NaV_8O_{20} nanobelts can be primarily ascribed to the pre-insertion of Na^+ ions during synthesis. This pre-insertion enhances the redox active sites, provides an efficient diffusion path for Na^+ ions, and ensures optimal interlayer spacing, facilitating effective Na^+ ion intercalation. Additionally, the high electrical conductivity of the NaV_8O_{20} nanobelts further improves their overall electrochemical behaviour, leading to enhanced charge storage and cyclic stability. These features collectively position NaV_8O_{20} nanobelts as an auspicious material for next-generation energy storage technologies.

Table 1 Comparative study of NaV_8O_{20} electrode and ASC device with previously reported metal vanadate electrodes and devices

Vanadate material	Method	Morphology	Three-electrode system			Supercapacitor device				Ref.
			Electrolyte	C_{sp} (F g^{-1} @ A g^{-1})	Electrode stability (% @ cycles)	Voltage window (V)	E_d (W h kg^{-1})	P_d (W kg^{-1})	Device stability (% @ cycles)	
$LiVO_3$	Chemical route	Nanorods	1 M Li_2SO_4	426 @ 0.5	80 @ 2000	1.6	25	3600	80 @ 5000	40
Li_3VO_4/carbon	Solid-state	Nanofibers	0.1 mol per L $(NH_4)_2SO_4$	—	—	3.8	110	3870	86 @ 2400	41
β-$Na_{0.33}V_2O_5$	Hydrothermal	Nanobelts	1 M $LiCO_4$/PC	320 @ 5 mV s^{-1}	—	1	47	5000	66 @ 4000	42
β-$Na_{0.33}V_2O_5$	Spin coating	Nanowires	1 M $LiCO_4$/PC	498 @ 0.4	90 @ 1500	—	—	—	—	43
NaV_3O_8	Electrochemical conversion	Nanosheets	1 M Na_2SO_4	640.10 @ 0.5	87.7 @ 2000	1.6	62.6	7200	81 @ 5000	44
$Na_2V_6O_{16}$	Chemical route	Nanobelts	1 M Na_2SO_4	455 @ 0.5	90 @ 5000	1.6	42	4300	80 @ 5000	27
$Na_6V_{10}O_{28}$	Chemical route	Microrods	1 M $LiClO_4$ + PC	354 @ 0.1	—	2.8	73	6238	70 @ 5000	45
KV_3O_8	Chemical route	Nanobelts	0.5 M K_2SO_4	677 @ 0.5	89 @ 5000	1.8	51	4127	90 @ 5000	46
$Cu_3V_2O_8$	SILAR	Nanopebbles	1.5 M $NaClO_4$	443 @ 5 mV s^{-1}	85 @ 2000	1.15	8.4	345	76 @ 4000	47
S–$Co_3V_2O_8$	Hydrothermal	Nanosheets	6 M KOH	410 mA h g^{-1} at 2A g^{-1}	94 @ 4000	1.5	36	11 600	98 @ 4000	48
$Mn_2V_2O_7$	Hydrothermal	Nanoparticles	3 M KOH	327 C g^{-1} at 1 A g^{-1}	93 @ 10 000	1.5	44.3	807.4	158 @ 10 000	49
$Ni_{3-x}Co_xV_2O_8$	Hydrothermal	Oval-shaped	3 M KOH	391 @ 0.5	98 @ 8000	1.3	25.5	7500	85 @ 10 000	50
$Ni_3V_2O_8$/Ni	Hydrothermal	Nanosheets	3 M KOH	1300 @ 1	80 @ 7000	1.2	33.2	2400	73 @ 10 000	51
$NiCo_2V_2O_8$	Microwave-assisted	Microspheres	2 M KOH	113.2 mA h g^{-1} at 0.5 A g^{-1}	82 @ 10 000	1.6	34.8	4000	80 @ 10 000	52
NaV_8O_{20}	**Hydrothermal**	**Nanobelts**	**1 M Na_2SO_4**	**676 @ 0.5**	**90 @ 10 000**	**1.6**	**45**	**5224**	**89 @ 10 000**	**This work**

4.3 Practical application of the AC//NaV_8O_{20} ASC coin cell device

Fig. 7 displays the AC//NaV_8O_{20} ASC coin cell device for its practical application by glowing the 28-red LED-contained panel. Each red LED bulb requires 1.2 V to shine; therefore, two AC//NaV_8O_{20} coin cell devices were connected in series for lighting. Then, fabricated ASC coin cell devices were first charged up to 1.6 V and discharged through an LED panel. These two devices can easily illuminate LED panels up to ~120 s (ESI Media File†), demonstrating the successful practical applicability of NaV_8O_{20} nanobelts material for SC application.

4.4 Electrochemical performance of NaV_8O_{20} nanobelts for Na^+ ion battery

To identify the electrochemical features of the NaV_8O_{20} nanobelts for the Na-ion battery, half-cell devices were assembled using Na metal foil as the reference/counter electrode. Fig. 8 shows the electrochemical measurements of a fabricated Na-ion battery performed in the voltage range of 1.5–4.0 V *vs.* Na/Na^+ to investigate the electrochemical redox reaction kinetics of the NaV_8O_{20} nanobelts. Fig. 8a shows the initial three CV curves recorded at a scan rate of 0.1 mV s^{-1} *vs.* Na/Na^+. These CV curves show a significant degree of overlap, particularly during the initial three cycles, indicating excellent reversibility of Na^+ ion insertion/extraction between the electrodes. The CV profiles exhibit two distinct intercalation peaks at 1.997 V and 3.631 V, along with two corresponding de-intercalation peaks at 3.528 V and 1.75 V. These peaks are associated with the reversible intercalation and de-intercalation of Na^+ ions within the NaV_8O_{20} structure, contributing to the material's high-capacity retention. Along with this, some minor oxidation peaks (3.075 and 3.204 V) and reduction (2.783 and 2.991 V) peaks were observed. These peaks may arise due to the multistep process of Na^+ ions insertion and de-insertion.[53,54]

The CV measurements for 0.1 to 1 mV s^{-1} scan rates were also performed (ESI, Fig. S3(e)†) to examine the rate performance and reaction kinetics. Fig. S3(e)† indicates that the peak positions slightly shift towards higher potentials, specifying that the Na^+ ions' insertion and de-insertion kinetics are closely related at different scan rates. To evaluate the Na^+ ions diffusion characteristics for the NaV_8O_{20} electrode material, the diffusion coefficient (D) is determined by the Randles–Sevcik equation:[55]

$$i_p = 0.4463 \times n \times F \times C \times A \times \left[\frac{nF\theta D}{RT}\right]^{\frac{1}{2}} \quad (3)$$

where i_p is the peak current, n is the electron density, C is the electrolyte molar concentration, F is Faraday's constant (C mol^{-1}), A is an electroactive area of an electrode (cm^2), D is the diffusion coefficient of a redox mediator (cm^2 s^{-1}), θ is the scan rate (mV s^{-1}), R is the gas constant (J K^{-1} mol^{-1}) and T is the temperature (K).

To calculate D from the CV measurements, the above formula can be modified as follows:

$$\frac{i_p}{\theta^{1/2}} = 2.69 \times 10^5 \times A \times C \times D^{1/2} \times n^{1/2} \quad (4)$$

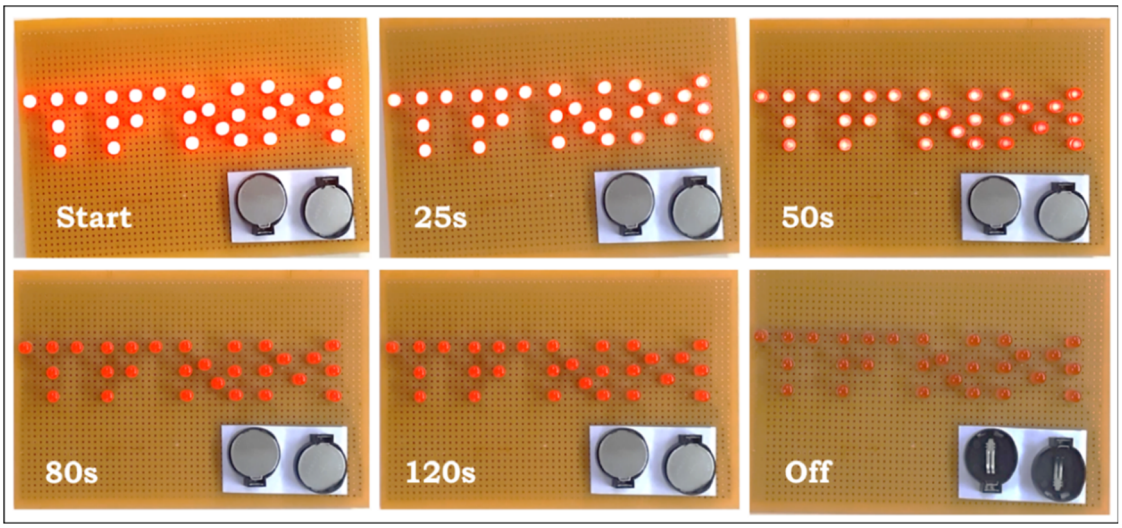

Fig. 7 Device demonstration of the AC//NaV_8O_{20} ASC coin cell device.

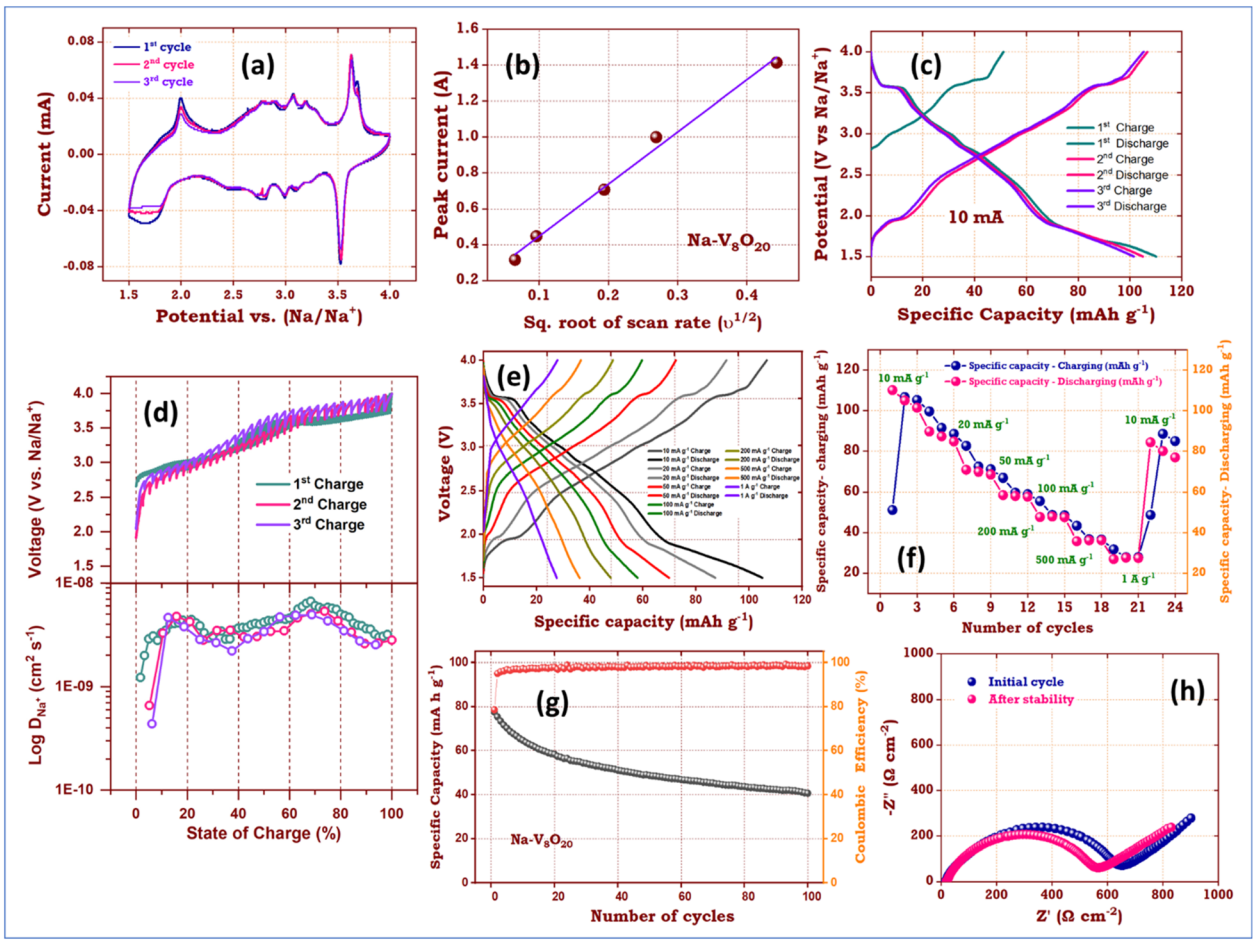

Fig. 8 (a) Initial three CV profiles at 0.1 mV s^{-1} between 1.5-4.0 V, (b) peak current *vs.* square root of the scan rates, (c) galvanostatic charge/discharge curves at 10 mA g^{-1}, (d) galvanostatic intermittent titration technique (GITT) profile and corresponding the diffusion coefficient of Na^+ ions and corresponding the diffusion coefficient of sodium ions during 1st, 2nd and 3rd charge at 100 mA g^{-1} for 300 s followed by 2 h, (e) GCD curves with different current densities from 10 to 1000 mA g^{-1}, (f) rate capability plot, (g) cycling performance at a current density of 100 mA g^{-1} and (h) Nyquist plot Na-ion battery device.

Table 2 Summary of diffusion coefficient of various sodium-ion cathode materials reported in the literature with our work

Electrode material	Current density	GITT-pulse duration/relaxation time	Diffusion coefficient (D_{Na^+})	Ref.
$NaVPO_4F$	14.3 mA g^{-1}	600 s/2 h	10^{-11} to 10^{-10} cm^2 s^{-1}	57
$Na_3MnTi(PO_4)_3$	11.7 mA g^{-1}	10 min/30 min	10^{-10} to 10^{-15} m^2 s^{-1}	58
Fe-HCF (iron-based hexacyanoferrate)	—	600 s/2 h	$\sim10^{-11}$ cm^2 s^{-1}	59
$NaFePO_4$	3.85 mA g^{-1}	1 h/15 h	$\sim10^{-17}$ cm^2 s^{-1}	60
$Na_{0.66}Ca_{0.05}[Ni_{0.25}Li_{0.11}Mn_{0.64}]O_{1.95}F_{0.05}$	13 mA g^{-1}	30 min/5 h	10^{-11} to 10^{-12} cm^2 s^{-1}	61
$Na_8Fe_5(SO_4)_9$@rGO	—	—	10^{-11} to 10^{-12} cm^2 s^{-1}	62
NaV_8O_{20}	**100 mA g^{-1}**	**300 s/2 h**	**$\sim10^{-9}$ cm^2 s^{-1}**	**This work**

where, $\frac{i_p}{\theta^{1/2}}$ is the slope of the plot of peak current *vs.* the square root of the scan rate (Fig. 8b). Using this formula, the calculated Na^+ ions diffusion coefficient value of the NaV_8O_{20} cathode material was found to be 4.10×10^{-7} cm^2 s^{-1}, reflecting faster Na^+ ion diffusion inside NaV_8O_{20} cathode material. This excellent diffusion coefficient value results from (1) 1D nanobelts morphology and high surface area of NaV_8O_{20} nanobelts material, which provides a long pathway for easier ion migration, and (2) high electrical conductivity, which is helpful for an efficient charge transfer process. Fig. 8c displays the GCD plot of the NaV_8O_{20} material at a 10 mA g^{-1} of current densities for the initial three cycles. Here, the plateaus are well corroborated with the CV curves and possess a maximum reversible discharge capacity of 110 mA h g^{-1}. These three GCD curves slightly overlapped, which showed excellent ionic diffusion features and structural stability, complementing the electronic conductivity of the NaV_8O_{20} cathode material. The galvanostatic intermittent titration technique (GITT) was performed to analyze the diffusion kinetics of Na^+ ions. During the measurement, closed-circuit voltage (CCV) was obtained by applying a current pulse of 100 mA g^{-1} for 300 s, followed by a relaxation period of 2 h to measure the quasi-open circuit voltage (QOCV). The diffusion coefficient of sodium ions (D_{Na^+}) of NaV_8O_{20} was calculated from the obtained GITT data according to the following formula:

$$D = \frac{4}{\pi\tau}\left(\frac{n_m V_m}{S}\right)^2\left(\frac{\Delta E_s}{\Delta E_t}\right)^2 \quad (5)$$

where τ is the duration of the current pulse (s), $n_m$is the number of moles of active material (mol), V_m is the molar volume of the electrode (cm^3 mol^{-1}), S is the electrolyte/electrode contact area (cm^2), ΔE_s is the steady-state voltage change due to the current pulse, and ΔE_t is the voltage change during titration.[56] The obtained D_{Na^+} values range from 4.4×10^{-10} cm^2 s^{-1} to 6.6×10^{-9} cm^2 s^{-1}, suggesting the effective diffusion of Na^+ ions. For comparison, the diffusion coefficients of various sodium ion cathode materials are summarized in Table 2. The comparative table implies that the 1D and nanobelt morphology of the NaV_8O_{20} electrode significantly enhances the diffusion of Na^+ ions compared to the other reported materials, highlighting its potential in high-efficiency sodium-ion batteries.

Fig. 8e displays the GCD behavior of second cycles for different rates from 10 mA g^{-1} to 1 A g^{-1}. The NaV_8O_{20} cathode provides a maximum discharge capacity of 105, 87, 70, 58, 48, 36, and 28 mA h g^{-1} for the current densities of 10, 20, 50, 100, 200, 500, and 1000 mA g^{-1}. Additionally, the rate capability of the NaV_8O_{20} cathode is shown in Fig. 8f; three cycles with each rate were tested, and the nature shows the electrochemical stability at a particular rate, but the capacity decreases with an increase in the rate. As the current density reverts to 10 mA g^{-1}, the NaV_8O_{20} cathode recovers ~83.2% (84 mA h g^{-1}) of its initial capacity. In addition, the cyclic stability measurement was performed over the fabricated Na^+ ion battery. Fig. 8g displays the cyclic stability of the Na^+ ion battery performed for 100 cycles at a current density of 100 mA g^{-1}. The Na^+ ion battery device displays ~100% coulombic efficiency while retaining ~52.4% of the initial capacity. The observed capacity fading can be attributed to the forming of a passivation layer on the electrode surface and a reduction in the number of electroactive sites. Additionally, EIS was employed to analyze the reaction kinetics of the NaV_8O_{20} cathode, both before and after cycling, as shown in Fig. 8h. By comparing both the EIS spectra, it can be found that the R_{ct} (quasi-semicircle) for the diffusion of sodium ions around ~650 Ω, which after cycling gradually decreased to ~562 Ω and shows an increase in ion and electron transport mobility as cycling is undertaken. This may be due to the decrease in the charge transfer characteristic in terms of lack of the electrolyte ions at the surface of the electrodes, activation, or reduction in active surface area during a prolonged cycling test.

5. Conclusions

In summary, we have successfully synthesized one-dimensional (1D) and layered sodium vanadate (NaV_8O_{20}) nanobelts using a simple, cost-effective hydrothermal method and demonstrated their dual application as high-performance electrode materials for SC and SIB devices. This study represents a significant advancement as it is the first to explore the electrochemical potential of NaV_8O_{20} nanobelts in both SCs and SIBs. Compared to previously reported metal vanadate-based electrode materials, the NaV_8O_{20} nanobelts exhibit remarkable electrochemical performance owing to their unique 1D and layered structure. This architecture significantly improves the electrochemical properties, leading to excellent cycling stability and superior rate performance for both SCs and SIBs. For SCs, the NaV_8O_{20} nanobelts exhibit an impressive C_{sp} of 676 F g^{-1} at 0.5 A g^{-1} and remarkable cyclic stability, retaining ~90% of the

capacitance after 10 000 cycles. Moreover, the ASC coin cell device (AC//NaV_8O_{20}) delivers an optimal E_d of 45 W h kg^{-1} and P_d of 5224.48 W kg^{-1}, with 89% cyclic stability after 10 000 cycles, demonstrating its suitability for high-performance energy storage systems. In addition to SCs, the NaV_8O_{20} nanobelts were employed as a cathode material for SIBs, showing a high initial charge/discharge capacity of 110 mA h g^{-1} and a retention of 52.4% capacity after 100 cycles at 100 mA g^{-1}. The GITT measurements reveal a high diffusion coefficient for Na^+ ions, indicating that the NaV_8O_{20} nanobelts enable efficient ion transport during cycling, which is essential for high-rate performance and long-term stability. These results highlight the potential of NaV_8O_{20} nanobelts for dual electrochemical applications, with a simple synthesis process which is both practical and sustainable.

Data availability

The data supporting this article have been included as part of the ESI.†

Conflicts of interest

There are no conflicts to declare.

Acknowledgements

The authors express their gratitude to the Alexander von Humboldt Foundation for donating the potentiostat. ASV is thankful to Symbiosis International (Deemed University), Pune for the financial support provided through the Major Research Project (MJRP) grant (2024/4900). SSW acknowledges support from the SERB-TARE project (TAR/2020/000257) funded by the Department of Science and Technology (DST), India. SAS extends appreciation to the DST, Government of India, for the PhD fellowship provided under the DST-INSPIRE scheme. Also, this research was supported by Basic Science Research Program through the National Research Foundation of Korea (NRF) funded by the Ministry of Education (No. RS-2019-NR040081).

References

1 R. Rajagopalan and L. Zhang, *Advanced Materials for Sodium Ion Storage*, CRC Press, 2019.
2 M. Wu, X. Hu, W. Zheng, L. Chen and Q. Zhang, *Chem. Eng. J.*, 2023, **466**, 143077.
3 S. Kumar, G. Saeed, L. Zhu, K. N. Hui, N. H. Kim and J. H. Lee, *Chem. Eng. J.*, 2021, **403**, 126352.
4 H. Sun, Y. Zhang, J. Zhang, X. Sun and H. Peng, *Nat. Rev. Mater.*, 2017, **2**, 17023.
5 L. Yu, X. He, B. Peng, F. Wang, N. Ahmad, Y. Shen, X. Ma, Z. Tao, J. Liang and Z. Jiang, *Adv. Funct. Mater.*, 2024, **34**, 2406771.
6 Q. Li, D. Yang, H. Chen, X. Lv, Y. Jiang, Y. Feng, X. Rui and Y. Yu, *SusMat*, 2021, **1**, 359–392.
7 G. Wan, Y. Chen, B. Peng, L. Yu, X. Ma, N. Ahmad and G. Zhang, *Battery Energy*, 2023, **2**, 20230022.
8 Y. F. Zhu, Y. Xiao, S. X. Dou, Y. M. Kang and S. L. Chou, *Escience*, 2021, **1**, 13–27.
9 A. Navarro-Suárez, J. Carretero-González, N. Casado, D. Mecerreyes, T. Rojo and E. Castillo-Martinez, *Sustainable Energy Fuels*, 2018, **2**, 836–842.
10 P. Mutadak, A. Vedpathak, S. Warule, N. Chaudhari, S. Sartale, M. More and D. J. Late, *Nanoscale Horiz.*, 2024, **9**, 2259–2272.
11 B. B. Sahoo, V. S. Pandey, A. S. Dogonchi, P. K. Mohapatra, D. N. Thatoi, N. Nayak and M. K. Nayak, *J. Energy Storage*, 2023, **65**, 107335.
12 I. Melkiyur, Y. Rathinam, P. S. Kumar, A. Sankaiya, S. Pitchaiya, R. Ganesan and D. Velauthapillai, *Renewable Sustainable Energy Rev.*, 2023, **173**, 113106.
13 A. D. Narang, S. P. Gupta, P. P. Sanap, S. S. Kahandal, R. S. Tupke, H. Kim, Q. Wang, A. S. Vedpathak, S. D. Sartale and V. K. Gade, *J. Mater. Sci.: Mater. Electron.*, 2024, **35**, 1335.
14 D. Xia, H. Gao, M. Li, F. Gong and M. Li, *Energy Storage Mater.*, 2021, **35**, 169–191.
15 G. Yao, N. Zhang, Y. Zhang and T. Zhou, *J. Nanopart. Res.*, 2021, **23**, 57.
16 G. Yang, H. Cui, G. Yang and C. Wang, *ACS Nano*, 2014, **8**, 4474–4487.
17 A. Mishra, G. Bera, P. Mal, G. Padmaja, P. Sen, P. Das, B. Chakraborty and G. Turpu, *Appl. Surf. Sci.*, 2019, **488**, 221–227.
18 Y. Piffard, F. Leroux, D. Guyomard, J.-L. Mansot and M. Tournoux, *J. Power Sources*, 1997, **68**, 698–703.
19 C. Lv, J. Sun, G. Chen, C. Yan and D. Chen, *Nano Energy*, 2017, **33**, 138–145.
20 M. Li, Y. Gao, N. Chen, X. Meng, C. Wang, Y. Zhang, D. Zhang, Y. Wei, F. Du and G. Chen, *Chem.–Eur. J.*, 2016, **22**, 11405–11412.
21 Y. Wang, H. Chai, H. Dong, J. Xu, D. Jia and W. Zhou, *ACS Appl. Mater. Interfaces*, 2016, **8**, 27291–27297.
22 Y. Zhang, X. Xu, Y. Gao, D. Gao, Z. Wei and H. Wu, *J. Power Sources*, 2020, **455**, 227985.
23 Q. Wei, Q. Wang, Q. Li, Q. An, Y. Zhao, Z. Peng, Y. Jiang, S. Tan, M. Yan and L. Mai, *Nano Energy*, 2018, **47**, 294–300.
24 A. Sarkar, S. Sarkar and S. Mitra, *J. Mater. Chem. A*, 2017, **5**, 24929–24941.
25 W. Avansi, C. Ribeiro, E. R. Leite and V. R. Mastelaro, *Mater. Chem. Phys.*, 2011, **127**, 56–61.
26 M. Du, C. Liu, F. Zhang, W. Dong, X. Zhang, Y. Sang, J. J. Wang, Y. G. Guo, H. Liu and S. Wang, *Advanced Science*, 2020, **7**, 2000083.
27 A. Vedpathak, T. Shinde, M. A. Desai, B. R. Thombare, R. Humane, S. A. Raut, R. Kalubarme, S. D. Sartale and S. Bhagwat, *ACS Appl. Energy Mater.*, 2023, **6**, 4693–4703.
28 J. Mao, C. He, J. Qi, A. Zhang, Y. Sui, Y. He, Q. Meng and F. Wei, *J. Electron. Mater.*, 2018, **47**, 512–520.
29 M. Aureliano and D. C. Crans, *J. Inorg. Biochem.*, 2009, **103**, 536–546.
30 P. Chithaiah, G. Chandrappa and J. Livage, *Inorg. Chem.*, 2012, **51**, 2241–2246.

31 C.-J. Mao, H.-C. Pan, X.-C. Wu, J.-J. Zhu and H.-Y. Chen, *J. Phys. Chem. B*, 2006, **110**, 14709–14713.
32 Y. Gogotsi and R. M. Penner, *ACS Nano*, 2018, **12**, 2081–2083.
33 S. Ardizzone, G. Fregonara and S. Trasatti, *Electrochim. Acta*, 1990, **35**, 263–267.
34 C. V. Khedkar, A. S. Vedpathak, A. V. Dhotre, K. D. Daware, Y. D. Kolekar, S. D. Sartale, S. W. Gosavi and S. I. Patil, *Chem. Phys. Impact*, 2023, **6**, 100153.
35 T. Liu, H. Chai, D. Jia, Y. Su, T. Wang and W. Zhou, *Electrochim. Acta*, 2015, **180**, 998–1006.
36 D. Sun, J. Lang, X. Yan, L. Hu and Q. Xue, *J. Solid State Chem.*, 2011, **184**, 1333–1338.
37 A. S. Vedpathak, M. A. Desai, S. Bhagwat and S. D. Sartale, *Energy Fuels*, 2022, **36**, 4596–4608.
38 M. A. Desai, A. S. Vedpathak, A. R. Bhapkar, G. D. Saratale and S. D. Sartale, *J. Environ. Manage.*, 2021, **299**, 113564.
39 C. Jagtap, V. Kadam, B. Kamble, P. Lokhande, A. Pakdel, D. Kumar, R. Udayabhaskar, A. Vedpathak, N. Chaure and H. Pathan, *J. Energy Storage*, 2024, **83**, 110666.
40 T. N. Shinde, A. Vedpathak, B. J. Nagare, D. M. Sapkal, M. Desai, P. P. Atre and S. D. Sartale, *Energy Technol.*, 2024, **12**, 2301056.
41 F. Wang, Z. Liu, X. Yuan, J. Mo, C. Li, L. Fu, Y. Zhu, X. Wu and Y. Wu, *J. Mater. Chem. A*, 2017, **5**, 14922–14929.
42 E. Khoo, J. Wang, J. Ma and P. S. Lee, *J. Mater. Chem.*, 2010, **20**, 8368–8374.
43 N. T. H. Trang, N. Lingappan, I. Shakir and D. J. Kang, *J. Power Sources*, 2014, **251**, 237–242.
44 A. Vedpathak, M. Desai, B. Thombare, R. S. Kalubarme, G. Guan, S. Bhagwat and S. D. Sartale, *J. Electroanal. Chem.*, 2024, **958**, 118150.
45 H. Y. Chen, G. Wee, R. Al-Oweini, J. Friedl, K. S. Tan, Y. Wang, C. L. Wong, U. Kortz, U. Stimming and M. Srinivasan, *ChemPhysChem*, 2014, **15**, 2162–2169.
46 A. S. Vedpathak, S. S. Kalyane, T. N. Shinde, Q. Wang, R. N. Bulakhe, J. M. Kim and S. D. Sartale, *J. Power Sources*, 2024, **621**, 235315.
47 S. R. Sankapal, T. B. Deshmukh, A. G. Bagde, K. Patil, B. R. Sankapal and C. D. Lokhande, *J. Phys. Chem. Solids*, 2024, **195**, 112286.
48 G. P. Sharma, P. K. Gupta, S. K. Sharma, R. G. S. Pala and S. Sivakumar, *ACS Appl. Energy Mater.*, 2021, **4**, 4758–4771.
49 K. Prasad, T. Sreekanth, K. Yoo and J. Kim, *Inorg. Chem. Commun.*, 2024, **159**, 111848.
50 D. Merum, N. Parvin, S. V. P. Vattikuti, R. R. Nallapureddy, R. Pitcheri, M. Shkir, M. A. Manthrammel, A. N. Banerjee and S. W. Joo, *J. Energy Storage*, 2023, **61**, 106674.
51 D. Merum, R. R. Nallapureddy, M. R. Pallavolu, T. K. Mandal, R. R. Gutturu, N. Parvin, A. N. Banerjee and S. W. Joo, *ACS Appl. Energy Mater.*, 2022, **5**, 5561–5578.
52 H. Sun, Y. Li, H. Chai, Y. Cao and W. Zhou, *J. Alloys Compd.*, 2019, **805**, 388–395.
53 J. Cheng, G. Gu, Q. Guan, J. M. Razal, Z. Wang, X. Li and B. Wang, *J. Mater. Chem. A*, 2016, **4**, 2729–2737.
54 J. K. Kim, B. Senthilkumar, S. H. Sahgong, J. H. Kim, M. Chi and Y. Kim, *ACS Appl. Mater. Interfaces*, 2015, **7**, 7025–7032.
55 A. J. Bard, L. R. Faulkner and H. S. White, *Electrochemical Methods: Fundamentals and Applications*, John Wiley & Sons, 2022.
56 Y. Lu, C. Z. Zhao, R. Zhang, H. Yuan, L. P. Hou, Z. H. Fu, X. Chen, J.-Q. Huang and Q. Zhang, *Sci. Adv.*, 2021, **7**, eabi5520.
57 S. D. Shraer, N. D. Luchinin, I. A. Trussov, D. A. Aksyonov, A. V. Morozov, S. V. Ryazantsev, A. R. Iarchuk, P. A. Morozova, V. A. Nikitina and K. J. Stevenson, *Nat. Commun.*, 2022, **13**, 4097.
58 S. Lu, Y. Cai, Y. Li, X. Du, J. Wang, Y. Liu, K. Cao and Y. Fan, *ACS Appl. Mater. Interfaces*, 2024, **16**, 38092–38100.
59 J. Zhong, L. Xia, S. Chen, Z. Zhang, Y. Pei, H. Chen, H. Sun, J. Zhu, B. Lu and Y. Zhang, *Proc. Natl. Acad. Sci. U. S. A.*, 2024, **121**, e2319193121.
60 Y. Zhu, Y. Xu, Y. Liu, C. Luo and C. Wang, *Nanoscale*, 2013, **5**, 780–787.
61 Z. Y. Li, X. Ma, K. Sun, F. Ning, L. Sun, G. Tian, J. Gao, H. Wang and D. Chen, *J. Mater. Chem. A*, 2024, **12**, 26113–26124.
62 C. Liu, K. Chen, H. Xiong, A. Zhao, H. Zhang, Q. Li, X. Ai, H. Yang, Y. Fang and Y. Cao, *eScience*, 2024, **4**, 100186.

